Additive Manufacturing of Biomechanically Tailored Meshes for Compliant Wearable and Implantable Devices

As Published: 10.1002/ADFM.201901815

Publisher: Wiley

Persistent URL: https://hdl.handle.net/1721.1/134769

Version: Author's final manuscript: final author's manuscript post peer review, without publisher's formatting or copy editing

Additive Manufacturing of Biomechanically Tailored Meshes for Compliant Wearable and Implantable Devices

*Sebastian W. Pattinson,[*] Meghan E. Huber, Sanha Kim, Jongwoo Lee, Sarah Grunsfeld, Ricardo Roberts, Gregory Dreifus, Christoph Meier, Lei Liu, Neville Hogan, A. John Hart**

Dr. S. W. Pattinson, Dr. M. E. Huber, Dr. S. Kim, Mr. J. Lee, Ms. S. Grunsfeld, Dr. R. Roberts, Mr. G. Dreifus, Dr. C. Meier, Dr. L Liu, Prof. N. Hogan, Prof. A. J. Hart

Department of Mechanical Engineering, Massachusetts Institute of Technology, Cambridge, MA, United States.

Dr. S. W. Pattinson

Department of Engineering, University of Cambridge, Cambridge, United Kingdom.

Dr. S. Kim

Department of Mechanical Engineering, Korea Advanced Institute of Science and Technology, Daejeon, South Korea.

Ms. S. Grunsfeld

Department of Materials Science and Engineering, Massachusetts Institute of Technology, Cambridge, MA, United States.

Dr. R. Roberts

School of Engineering and Sciences, Tecnologico de Monterrey, Mexico

Prof. N. Hogan

Department of Brain and Cognitive Sciences, Massachusetts Institute of Technology, Cambridge, MA, United States.

Email: swp29@cam.ac.uk , ajhart@mit.edu

Keywords: Additive Manufacturing, Medical Devices, Biomechanics

Additive manufacturing (AM) of medical devices such as orthopedic implants and hearing aids is highly attractive because of AM's potential to match the complex form and mechanics of individual human bodies. Externally worn and implantable tissue-support devices, such as ankle or knee braces, and hernia repair mesh, offer a new opportunity for AM to mimic tissue-like mechanics and improve both patient outcomes and comfort. Here, it is demonstrated how explicit programming of the toolpath in an extrusion AM process can enable new, flexible mesh materials having digitally tailored mechanical properties and geometry. Meshes are fabricated by extrusion of thermoplastics, optionally with continuous fiber reinforcement, using a continuous toolpath that tailors the elasticity of unit cells of the mesh via incorporation of slack and modulation of filament-filament bonding. It is shown how the tensile mesh mechanics can be engineered to match the nonlinear response of muscle, incorporate printed mesh into an ankle brace with directionally specific inversion stiffness, and present further concepts for tailoring their 3D geometry for medical applications.

1. Introduction

Additive manufacturing (AM) enables the digitally-driven production of objects that are both individually customized and geometrically complex.[1] Considering the diversity and complexity of human bodies, AM is therefore well-suited to production of wearable and implantable devices

that offer enhanced performance or fit, including by customization, when compared to alternative fabrication methods. These advantages have already led to numerous additively manufactured medical devices, including orthopedic implants,[2] orthodontic aligners,[3] bone scaffolds,[4] and prostheses.[5] However, importantly, all of these AM-enhanced devices interface with rigid parts of the body, whereas soft tissues also often require mechanical support to prevent or heal injury.[6]

The mechanical characteristics of soft tissue support devices are critical to their performance. For example, conventionally manufactured ankle braces, which restrict movement to prevent (re-)injury can be bulky and poorly fitting. Implanted surgical mesh, which mechanically supports tissue as it heals following surgery and is used in many of the estimated 20 million hernia surgeries around the world every year,[7] can restrict abdominal wall mobility and lead to rigidity and discomfort.[8] These support devices could similarly benefit from the customization and complex geometries enabled by AM.

Producing devices that replicate the mechanics of soft tissues is challenging, though, because tissues such as muscle, tendons, and ligaments often have non-linear tensile stress-strain responses, with an initially low stiffness that increases rapidly as the tissue becomes taut.[9] The mechanical response of tissue is also highly anisotropic, varies significantly according to the tissue type, and can be different for individual patients according to their body type and health condition.[10] For instance, the tensile modulus of rat muscular tissue has been measured to be approximately 0.1 MPa until a strain of 20%, and ~2.6MPa beyond 40% strain; for connective tissue the relevant values are ~3 MPa to 10% strain and ~40MPa thereafter.[9] These tissues are found in close proximity to one another, meaning that the overall mechanical properties have spatially varying mechanics in addition to significant anisotropy. Additionally, soft tissue support devices should be sufficiently porous to enable breathability (in the case of an external device) or tissue integration (in the case of an implant).

Established methods to produce soft-tissue devices such as wearable braces and implantable mesh typically use conventional fabrics made by knitting or weaving. While there have been exciting innovations in conventional fabrics,[11],[12],[13] weaving is suited to regular patterns and cannot adapt to sharp gradients in mechanical properties, while the looped topologies used in knitting feature limited stiffness and control over 3D structure. Many researchers and designers have explored the utility of AM to produce fabric-like geometries, such as thin, continuous lattice structures or interlocked chainmail.[14],[15],[16],[17] Yet, adaptation of AM to produce soft tissue supports requires detailed consideration of the local and global mechanics necessary to provide meaningful utility, as well as design and toolpath planning algorithms capable of adaptation to complex 3D topologies that match the contours of the body.

Here, we present a new, versatile approach to digital fabrication of biomechanically tailored mesh materials using AM. The explicit programming of the toolpath of an extruded thermoplastic, alongside optional reinforcement by continuous fiber, enables the additive manufacturing of meshes with nonlinear elasticity to mimic the mechanics and conform to the 3D structure of soft tissue. We demonstrate the advantages of this method by manufacturing and testing an ankle brace that selectively prevents excessive inversion of the ankle, while leaving the ankle otherwise free to move naturally in all other directions. We show the further possibilities enabled by toolpath control in enhancing the conformity of the meshes to 3D structures by local patterning of Negative Poisson's Ratio structures as well as using non-planar toolpaths to modulate connectivity and to produce seamless 3-dimensional meshes.

2. Results and Discussion

To enable additive manufacturing of meshes with locally varying and anisotropic mechanics, we introduce a hierarchical design where each mesh consists of an array of cells (**Figure 1**). By

specifying the mechanical properties of a cell, we specify the local and global mechanics of the mesh. Each cell is composed of orthogonal elements, which determine the tensile response of each cell in its respective direction, and can therefore establish anisotropic response.

Extrusion additive manufacturing, specifically using a thermoplastic elastomer (see Methods) for demonstration herein, is chosen because of its simplicity and versatility. However, unlike typical extrusion AM implementations where bulk objects are built with rigid bases for attachment to the printer platform, here the mesh is directly printed as one or a few layers, with explicit control of the toolpath to specify the desired mechanical properties of the mesh. A continuous toolpath is important for mesh performance, because interruptions of the toolpath lead to local defects that can compromise strength and therefore are especially undesirable for medical applications. For meshes where each fiber running vertically or horizontally from one end of the mesh to the other has uniform thickness, the toolpath follows a raster-pattern where all horizontal lines are printed followed by the vertical lines. For meshes where a horizontal or vertical fiber features locally varying thickness, which allows the mesh to exhibit a greater range of local mechanical response, we use the graph theory-based toolpath planning algorithm developed by Dreifus et al.[18] This algorithm is able to plot complex toolpaths where the extruder passes over each part of the mesh a programmable number of times while minimizing discontinuities. Since the extruder deposits a uniform thickness of thermoplastic each time it passes over a section of the mesh, this allows for the local control of mesh thickness.

2.1 Engineering tissue-like mesh mechanics

To create printed mesh that accurately mimics the non-linear tensile response of soft tissue, we must be able to control the stiffness at small strains (low) and at large strains (high), and the transition strain at which the stiffness significantly increases (**Figure 2A,B**). For this, we take

inspiration from the wavy structure of collagen;[19] incorporating waves into each fiber segment allows it to be stretched with an effective stiffness initially dominated by bending of the wave, and then subsequently by stretching of the fiber once it is taut. Thus, for a single segment with two waves and a total projected length l_e, the axial stiffness can be tuned by varying wave amplitude (h_w) and width (l_w), relative to the total projected length which includes the straight segments as well. As such, we model the nonlinear stretching behavior of the hyperelastic fiber element as the superposition of the stretching of the straight and wavy segments. First, the axial stiffness of the straight portion under applied force (F_e) is represented by a Mooney-Rivlin model as[20]

$$\frac{F_e}{A_e C_1} = \left(1 + \frac{\mu_2}{\mu_1}\frac{1}{\lambda_{e,s}}\right)\left(\lambda_{e,s} - \frac{1}{\lambda_{e,s}^2}\right) \quad \text{(Equation 1)}$$

where μ_1 and μ_2 are material constants, A_e is the original cross-sectional area of the printed fiber, and $\lambda_{e,s}$ is the element extension. The extension displacement due to stretching is therefore given as

$$\delta_{e,s} = l_e\left(\lambda_{e,s} - 1\right) \quad \text{(Equation 2)}$$

On the other hand, the extension displacement due to bending (i.e., straightening) of the wavy segment, is

$$\delta_{e,b} = 4\times\left\{h_w^2 + \left(\frac{l_w}{2}\right)^2\right\}^{1/2}\left[\cos\theta - \cos\left(\operatorname{atan}\frac{2h_w}{l_w}\right)\right] \quad \text{(Equation 3)}$$

where θ is wave angle under tensile force of F_e, determined by the equilibrium of moments as

$$dF_e\left\{h_w^2 + \left(\frac{l_w}{2}\right)^2\right\}^{1/2} sin\theta \cong -K' d\theta \quad \text{(Equation 4)}$$

Here, we assume the bending stiffness of the wave is constant and given as K'. The total extension displacement δ_e is the summation of $\delta_{e,s}$ and $\delta_{e,b}$. (A detailed derivation of above equations are described in Supporting Information). Thus, compared to tensile loading of a

straight segment only (**Figure 2B**), the wavy element exhibits a transition between low stiffness (dominated by "opening" of the waves) at small strain, to higher stiffness at large strain (dominated by stretching). The transition between bending- and stretching-dominated response is also coincident with a maximum stiffness (**Figure 2C**). In **Figure 2E,F**, the estimated force-strain and stiffness-strain curves of the two-wave element are compared to measurements on printed samples. By changing the wave amplitude with all other parameters unchanged, we tailor the strain (in terms of percent elongation relative to the original projected length) at which the highest stiffness occurs, to above 40%.

To control the small strain stiffness we vary the extent of bonding between adjacent elements, which is simply accomplished by printing adjacent elements in contact or with a small lateral gap. Printing adjacent elements in contact causes the elements to become welded, thereby effectively increasing their thickness perpendicular to the direction of strain.[21] The small strain stiffness depends on the bending stiffness of the waves, and the bending stiffness increases in a non-linear manner with the thickness of the fiber. As a demonstration, in **Figure 2G-H** we study example units containing 5 parallel, wavy fiber elements; in one instance all 5 elements are printed with lateral gaps; in another, the 3 central fibers are bonded; and, in the final instance, all 5 fibers are bonded. When all fibers are bonded the stiffness is relatively constant around 110N/m, while when all fibers are unbonded the stiffness is 20N/m until 10% strain, at which point it rises to a maximum of 207N/m at 40% strain. The samples where 3 fibers are bonded feature intermediate stiffness values of 53N/m at 10% strain rising to 150N/m at 40% strain.

Also, importantly the tensile behavior of the printed thermoplastic elastomer is resilient under cyclic loading, and therefore the printed mesh elements can withstand repeated stretching and release. For instance, we found no perceptible change in the tensile response of wavy elements over 1800 cycles, to a peak strain of 32% (**Figure S1**). Furthermore, the fiber bending

stiffness, and therefore the low-strain stiffness, depends in a non-linear manner on fiber diameter. Therefore, if the fiber becomes large enough, the bending stiffness will become similar to the stretching stiffness, and the non-linear tensile behavior will no longer be observed.

This simple design allows the digital printing of mesh designs with mechanical behavior that both qualitatively and quantitatively emulates the anisotropic, non-linear elasticity of natural tissue. For instance, by tailoring the small strain and high strain stiffness, as well as the transition strain, we show printed elastomer mesh matching the tensile response of rat muscle tissue, in both orthogonal directions (**Figure 3A-B**).[22] In the direction perpendicular to the muscle fibril orientation, the mesh exhibits a relatively constant modulus of 685kPa, while parallel to the muscle fibrils the mesh features a modulus of 111kPa until a strain of 10%, and beyond 20% strain the modulus increases to 453kPa. Here, we applied a strain rate of 0.05%/minute, which was identical to that used by Takaza et al[22] for their tissue measurements.

Altogether, by the strategies described herein, printed unit cells can have tensile stiffness values spanning 5 orders of magnitude (**Figure 3C**), from 20kN/m to 0.5N/m, and, by controlling the geometry and connectivity of the fiber elements, the transition strain can be tuned as well. The highest stiffness is achieved by incorporating continuous fiber such as stainless steel wire into the mesh, as discussed in detail later.

2.2 A mesh-reinforced brace to prevent ankle inversion

As a demonstration of a potential application of the nonlinear, muscle-like mechanics of the printed mesh, we built a prototype brace to selectively reinforce the inversion stiffness of the human ankle while leaving it otherwise free to move naturally. Ankle inversion is one of the most common injuries in humans and often leads to residual problems such as ankle instability and

pain, especially after recurring sprains.[23],[24],[25],[26] As a result, soft or semi-rigid ankle braces (typically made of lycra/neoprene or nylon/polyester, respectively) are often used to prevent recurrent injuries after a mild/moderate ankle sprain.[27] However, these devices typically uncomfortably restrict most or all of the degrees of freedom of the ankle, which limits their use by patients, can cause muscle to atrophy leading to increased susceptibility to future injury, and also negatively affects sports performance.[28],[29]

Ankle braces that are anatomically customized, either directly to the patient or made in a variety of shapes and sizes, and having locally defined, non-linear, mechanics, could both restrict excessive motion in undesired directions (e.g., inversion) and ideally enable natural motion in other directions. We thus prototyped a device to selectively stiffen the ankle when it undergoes inversion (**Figure 4a**), including a strip of printed mesh placed on the outside of the ankle, such that it will experience tension when the ankle attempts to invert. Importantly, the extensibility and transition strain of the mesh were designed to allow a degree of inversion while stiffening significantly once this is exceeded. A brace was fabricated by fastening the mesh to an assembly of 3D printed components, enabling it to be fitted around a shoe and interfaced with the instrumented measurement device. This setup ensured a rigid attachment to the body and that the forces were transferred via the non-linear mesh. Finally, the wavy component of the mesh (which has the non-linear tensile response) is layered without bonding, to make it flexible in bending out of plane and therefore allowing it to buckle, so that it does not affect the stiffness in eversion.

We then measured the static component of multivariable ankle mechanical impedance, a generalization of ankle stiffness, with and without the mesh placed over the ankle joint. Using an Anklebot (Bionik Laboratories Corporation, Watertown, MA), the static torque-angle relation in the inversion/eversion (IE) and dorsiflexion/plantarflexion (DP) directions were simultaneously measured and used to estimate ankle stiffness in different directions within IE-DP space.[23]

Data from 4 subjects indicate that our brace is able to selectively increase the linear approximation of effective ankle stiffness in inversion while leaving it relatively unaffected in other directions (**Figure. 4C,D** and **Figure S4**). Across all 4 subjects, wearing the mesh increased the effective ankle stiffness by an average of 78.69% in the inversion direction and only by 14.27% in eversion, -1.59% in dorsiflexion, and -1.40% in plantarflexion. Moreover, the results show that the added stiffness is non-linear (**Figure 4D** and **Figure S4**). The torque required to achieve angular displacement in inversion is relatively similar whether or not a brace is worn up to ~1.5°, after which the stiffness of the ankle with the brace becomes steadily higher until it is approximately ~50% greater than that of the bare ankle at an inversion of 15°. These results suggest that meshes with non-linear tensile response are promising candidates for making future braces that only prevent motion that will lead to injury, while otherwise leaving the ankle to move freely. Such braces may have significant potential both as prophylactic braces as well as aiding rehabilitation by enabling patients to resume activities more quickly.

2.3 Printing fiber-reinforced mesh

Thermoplastic elastomer meshes can achieve widely tailored mechanical properties for use in devices such as the ankle brace described above. However, many potential applications of printed mesh—including implantable hernia mesh—will demand greater stiffness and strength. Specifically, the stiffness of a strained elastomer mesh depends on the cross-sectional area of its fibers and therefore is proportional to the amount of printed material. However, to treat injury of some connective tissues an even greater stiffness is needed in the large strain regime, preventing excessive deformations and, ultimately, failure; for contrast, see **Figure S2a** where one all-elastomer unit cell breaks at 2.4N.

A strategy to digitally fabricate stronger mesh is to incorporate synthetic fibers or threads into the printing process. AM of fiber-reinforced components is well-known, particularly via placing a thermoplastic-coated thread into the layers of 3D components such as mechanical fixtures and brackets.[30] While this gives components with significantly enhanced flexural rigidity and strength, for printing mesh it is desirable to leave the fiber unconstrained in the open areas of each unit cell, to enable it to become taut only at a critical strain where the highest stiffness is needed. In other words, a continuous fiber such as a fine metal wire is compliant in bending like printed thermoplastic filament, but much more rigid in tension.

To incorporate continuous fiber into mesh, we implement a second (unheated) nozzle on the extrusion 3D printer, and thread the fiber through the nozzle. This allows the deposition of continuous fiber without a thermoplastic sheath by instead using an adhesive substrate to passively pull fiber out of a nozzle (**Figure 5B-C** and Supporting Video). We place a film with adhesive on both sides onto the printer bed, and then extrude a layer of thermoplastic onto this, according to the thermoplastic mesh design but leaving gaps where continuous fiber is desired. We move the fiber nozzle over the substrate, causing the fiber to follow the path of the nozzle and stick to the adhesive. The continuous fiber is patterned such that it overlaps with the already extruded thermoplastic in some regions. In order to bond the fiber to the rest of the mesh, we deposit another layer of thermoplastic in an identical pattern to the first layer, which sandwiches the fiber. Here, we print stainless steel thread as the continuous fiber, which is impervious to the temperatures used for thermoplastic extrusion (~210°C). Many other fiber materials with suitable thermal stability could be used, such as carbon fiber and Kevlar.

Here, a mesh that permits a continuous toolpath is important to minimize need to cut the fiber. And, because the continuous fiber cannot change direction unless it is in contact with the adhesive substrate, the fiber nozzle must be very close to the print bed for accurate patterning.

Also, the cell must have a minimum curvature due to the forces that build up in the fiber during bending. Finally, there has to be overlap between continuous fiber and elastomeric matrix to allow the continuous fiber to be bonded to the mesh. Taking these into consideration, we designed the unit cell shown in **Figure 5D** for use with continuous fiber.

These unit cells exhibit greater large strain stiffness than is possible with the all-elastomer designs, while retaining a large open area. In particular, the tensile response (**Figure 5E**) of these unit cells is governed by the elastomer at small strains (180 N/m stiffness), and stiffens sharply when the steel fiber becomes taut (7.3kN/m). As with the all-elastomer unit cells, the strain at which this transition occurs can be controlled by the wave amplitude of the pre-made fiber, and the large strain stiffness is governed by the fiber properties. The ultimate strength depends on the mesh design and the continuity of fiber path, but can be limited by the fiber-polymer adhesive strength.

2.4 Towards conformal, customized mesh-based assistive devices

Looking forward to broader uses of digitally tailored mesh in wearable and implantable devices, another important capability is conformality to 3D surfaces, both for increased comfort as well as to controllably transfer mechanical forces. This will ultimately be achieved by more sophisticated planning algorithms that relate the desired shape and mechanics to the mesh topology, and plan the printer toolpath accordingly including via non-planar printing layers.[31] Toward this goal, we show three further capabilities: (1) controlling drape by modulating bonding between orthogonal filaments; (2) coupling in-plane and out-of-plane displacements via mesh cells with negative Poisson's ratio; and (3) printing mesh onto 3D templates.

Conventional textiles are highly conformable because the constituent fibers (both within individual threads and yarn, and within knits and weaves) can slip over one another. It was

explained earlier that slip is undesirable for precise control of in-plane stress and strain; however, it can be useful if placed locally to allow mesh conformality. In the printing process, we therefore locally enable fiber slip by lifting the printer nozzle as it passes over filament in the mesh, such that the newly printed filament cools before it contacts the underlying filament on the print bed (**Figure 6a**). Printing fibers that are not bonded significantly enhances the drape of an exemplary printed fabric. Comparing two otherwise identical specimens placed in a cantilever configuration, the unbonded fabric deflects vertically ~230% more than the bonded fabric. Over a sphere (here, a golf ball), the unbonded fabric wraps the sphere while the bonded one does not. Control of the Poisson's ratio at the unit cell-level can also allow the fabric to conform to a curved surface without folding.[32] As a demonstration, a printed mesh with locally negative Poisson's ratio is placed onto the author's knee (**Figure 6b**).[33] When the same mesh is stretched in-plane by hand, it can bulge upward (Supplementary Video), suggesting that inverse design of the mesh pattern can enable complex strain profiles to be followed.

Last, explicit control of the printing toolpath also enables the production of non-planar meshes (**Figure 6c**), providing another means for devices to conform to the body while maintaining the desired mechanics for biomechanical reinforcement. To print mesh for a glove-like brace on a hand, we first 3D print support structure designed to approximate the height and position of a knuckle. Next, we cover these knuckle templates with tape to prevent the extruded mesh from adhering to the support directly. A graph-theory based, algorithm developed in a separate study, is used to plan the toolpath over the prescribed boundary and curved topography, with a minimum number of discontinuities.[18] The mesh is then sewn to a glove, and is therefore designed to counteract spasticity (increased stiffness) by providing extension forces to a clenched fist, which can occur from neurological injuries such as acute ischemic stroke.[34]

3. Conclusion

We have demonstrated a route to digital tailoring of compliant mesh materials, which may find wide application in the design and manufacturing of wearable and implantable devices. Importantly, the printed mesh architecture enables engineered nonlinear mechanics that can mimic those of soft tissue and enable 3D conformality to the body. We demonstrate a process where explicit control of the printer toolpath, a hierarchical mesh design, and new hardware for patterning of continuous fibers enables the additive manufacture of parts with locally controlled mechanics matching those of individuals' soft tissue. Moreover, we demonstrate how our toolpath software enables the production of meshes with 3D structure that allows better conformability to the body through inter-fiber bonding control for improved drape, locally patterned negative Poisson's Ratio regions, and 3D toolpaths printed onto support structures. We produce an example ankle brace that shows the potential of controlled non-linear tensile response by letting the ankle move freely unless it inverts to an excessive extent, as well as a glove with an embedded mesh designed to conform to the hand. Inverse design of meshes, where mesh material and geometry are designed to generate desired properties would enable unprecedented novel devices that seamlessly interact with the body, and thereby improve the lives of countless patients suffering from conditions ranging from ankle or other joint sprain to hernia and tremors.

4. Experimental Section

Printing: Extrusion is done using a commercial 3D printer Printrbot Simple Metal. Thermoplastic Polyurethane (Ninjaflex) is the primary matrix material used, while stainless steel thread (0.4mm thick 3 ply thread, 316L alloy, Adafruit Industries) is the pre-made continuous fiber. For continuous fiber deposition, the substrate is made adhesive through the use of double-sided tape.

The nozzle used to guide the continuous fiber is a tapered nozzle from Nordson (product number). We printed a holder for the nozzle to sit next to the extruder as shown in **Figure S1**.

Toolpath planning: The toolpath is essential to achieving the best mechanics/morphology from the fabrics and therefore we wrote our own software in the Python language to do this. The software takes as input the desired array of unit cells in the mesh alongside printing parameters such as rate and temperature, and translates these into g-code, which are the instructions for the printer. The g-code output by the Python software is then input into Repetier-Host software as manual g-code, which passes the instructions to the printer.

Mechanical Testing: Tensile testing was conducted using an Instron 1125 machine with a 20000 lb. (2511-305) and a 100N load cell (Omega S-type). All tests were conducted taking 3000 data points per minute at a displacement rate of 5 mm min^{-1}. Flexural testing was carried out by attaching a mass to fibers or fabrics and measuring the vertical displacement.

Finite Element Modeling: For the modeling of individual fibers, a finite element formulation based on the so-called geometrically exact Simo-Reissner beam theory, incorporating the deformation modes of axial tension, shear, torsion and bending, has been applied. The formulation is geometrically non-linear and accounts for arbitrarily large displacements and rotations as well as for finite strains. The stress-strain relationship is based on an elastic constitutive law defined by Young's modulus and Poisson's ratio. All simulations have been conducted in a quasi-static manner employing the in-house finite element research code BACI developed at the Institute for Computational Mechanics at the Technical University of Munich.

Ankle measurements experimental setup: Four subjects (age: 27±4 yrs; gender: 3 male, 1 female) with no reported history of biomechanical or neuromuscular disorders participated in the experiment. All gave informed written consent before the experiment. The experimental protocol was reviewed and approved by the Institutional Review Board of the Massachusetts Institute of

Technology. Subjects wore a modified shoe and a knee brace on their right leg, to which the Anklebot was attached.[35] The knee brace was attached to the chair such that weight of the robot and leg were fully supported and the foot did not contact the ground (Figure 4a). Subjects were instructed to remain relaxed during the experiment.

Each trial consisted of 24 movements (an inward and outward motion along 12 equally-spaced directions in IE-DP space, with a nominal displacement amplitude of 15° in each direction at constant speed of 5°/s) (Figure 4b). The robot speed was selected to maintain a quasi-static relationship between measured torque and displacement and avoid evoking spindle-mediated stretch reflexes. For each movement, the robot moved the ankle along a commanded trajectory and recorded applied torque and actual angular displacement at 200 Hz sampling frequency.

Four trials were conducted in each of two conditions: *no mesh* and *mesh*. During trials in the *mesh* condition, one end of the mesh was attached to the knee brace and the other was attached to the shoe on the lateral side of shank, parallel to the tibia (Figure 4a).

Ankle Measurement Data Analysis: In each condition, a vector field, V, defined as

$$(\tau_{\mathrm{IE}}, \tau_{\mathrm{DP}}) = V(\theta_{\mathrm{IE}}, \theta_{\mathrm{DP}})$$

was approximated from measured multivariable torque–angle relation in IE-DP space for each individual subject. θ_{IE} and θ_{DP} are the angular displacements in the IE and DP directions, respectively, and τ_{IE} and τ_{DP} are the corresponding applied torques. Figure 4c shows 2D slices of the two vector fields (*mesh* and *no mesh*) in the inversion direction for two example subjects. As expected, the mesh added nonlinear stiffness to the ankle.

To evaluate the directional effect of the mesh, ankle stiffness was also evaluated for all directions in each condition (*mesh* and *no mesh*). Ankle stiffness for a given direction was calculated as the slope of a linear approximation of the vector field in that direction.

Supporting Information

Supporting Information is available from the Wiley Online Library or from the author.

Acknowledgements

Financial support was provided by a National Science Foundation Science, Engineering, and Education for Sustainability postdoctoral fellowship (Award number: 1415129) to S.W.P.; a Samsung Scholarship to J.L; the School of Engineering and Sciences from Tecnologico de Monterrey to R.R.; the Manufacturing Demonstration Facility, Oak Ridge National Laboratory, the Department of Energy, UT-Batelle, Oak Ridge Associated Universities, the DOE's Advanced Manufacturing Office to G.D.; the German Academic Exchange Service (DAAD) to C.M.; and the Eric P. and Evelyn E. Newman Fund and NSF-CRCNS-1724135 to N.H. We would also like to acknowledge helpful discussions with Adam Stevens and Abhinav Rao.

Competing Interests

S.W.P. and A.J.H. are inventors on an MIT patent application: Systems, Devices, and Methods for Extrusion-Based Three-Dimensional Printing. U.S. Ser. No. 15/376,416. PCT Ser. No. PCT/US16/66205. This application primarily addresses the printing process for the mesh. S.W.P., A.J.H., M.E.H., J.L., and R.R. are also inventors on an MIT provisional patent application: Additively Manufactured Mesh Materials, Wearable and Implantable Devices, and Systems and Methods for Manufacturing the Same, U.S. Ser. No. 62/797,044. This application primarily addresses applications for the mesh.

Received: ((will be filled in by the editorial staff))
Revised: ((will be filled in by the editorial staff))
Published online: ((will be filled in by the editorial staff))

401 References

402 [1] S. Patra, V. Young, *Cell Biochem. Biophys.* **2016**, *74*, 93.

403 [2] S. L. Sing, J. An, W. Y. Yeong, F. E. Wiria, *J. Orthop. Res.* **2016**, *34*, 369.

404 [3] M. Martorelli, S. Gerbino, M. Giudice, P. Ausiello, *Dent. Mater.* **2013**, *29*, e1.

405 [4] R. Trombetta, J. A. Inzana, E. M. Schwarz, S. L. Kates, H. A. Awad, *Ann. Biomed. Eng.*
406 **2017**, *45*, 23.

407 [5] Y. He, G. Xue, J. Fu, *Sci. Rep.* **2015**, *4*, 6937.

408 [6] P. P. Pott, M. L. R. Schwarz, R. Gundling, K. Nowak, P. Hohenberger, E. D. Roessner,
409 *PLoS One* **2012**, *7*, 1.

410 [7] A. Kingsnorth, K. LeBlanc, *Lancet* **2003**, *362*, 1561.

411 [8] K. Junge, U. Klinge, A. Prescher, P. Giboni, M. Niewiera, V. Schumpelick, *Hernia* **2001**,
412 *5*, 113.

413 [9] B. Calvo, A. Ramirez, A. Alonso, J. Grasa, F. Soteras, R. Osta, M. J. Munoz, *J. Biomech.*
414 **2010**, *43*, 318.

415 [10] M. Śmietański, K. Bury, A. Tomaszewska, I. Lubowiecka, C. Szymczak, *Surg. Endosc.*
416 *Other Interv. Tech.* **2012**, *26*, 1461.

417 [11] J. Mccann, J. Mankoff, J. Hodgins, **2011**, *35*, 1.

418 [12] B. Bickel, B. Moritz, M. A. Otaduy, H. R. Lee, W. Matusik, **2009**.

419 [13] M. Akbari, A. Tamayol, S. Bagherifard, L. Serex, P. Mostafalu, N. Faramarzi, M. H.
420 Mohammadi, A. Khademhosseini, *Adv. Healthc. Mater.* **2016**, n/a.

421 [14] A. Johnson, G. A. Bingham, D. I. Wimpenny, *Rapid Prototyp. J.* **2013**, *19*, 199.

[15] J. White, M. Foley, A. Rowley, *3D Print. Addit. Manuf.* **2015**, *2*, 145.

[16] H. Peng, J. Mankoff, S. E. Hudson, J. Mccann, **2015**.

[17] P. Bettini, G. Alitta, G. Sala, L. Di Landro, *J. Mater. Eng. Perform.* **2017**, *26*, 843.

[18] G. Dreifus, K. Goodrick, S. Giles, M. Patel, R. M. Foster, C. Williams, J. Lindahl, B. Post, A. Roschli, L. Love, V. Kunc, *3D Print. Addit. Manuf.* **2017**, *4*, 98.

[19] T. Ushiki, *Arch. Histol. Cytol.* **2002**, *65*, 109.

[20] A. Bower, *Applied Mechanics of Solids*; CRC Press, 2009.

[21] J. E. Seppala, S. Hoon Han, K. E. Hillgartner, C. S. Davis, K. B. Migler, *Soft Matter* **2017**, *13*, 6761.

[22] M. Takaza, K. M. Moerman, J. Gindre, G. Lyons, C. K. Simms, *J. Mech. Behav. Biomed. Mater.* **2012**, *17*, 209.

[23] C. Doherty, E. Delahunt, B. Caulfield, J. Hertel, J. Ryan, C. Bleakley, *Sport. Med.* **2014**, *44*, 123.

[24] L. Tanen, C. L. Docherty, B. Van Der Pol, J. Simon, J. Schrader, *Foot Ankle Spec.* **2014**, *7*, 37.

[25] and D. C. T. J. P. Gerber, G. N. Williams, C. R. Scoville, R. A. Arciero, *Foot Ankle Int.* **1998**, *19*, 653.

[26] M. S. Yeung, K. M. Chan, C. H. So, W. Y. Yuan, *Br. J. Sports Med.* **1994**, *28*, 112.

[27] E. Eils, C. Demming, G. Kollmeier, L. Thorwesten, K. Völker, D. Rosenbaum, *Clin. Biomech.* **2002**, *17*, 526.

[28] L. Deberg, M. T. Andani, M. Hosseinipour, M. Elahinia, *Smart Mater. Res.* **2014**, 572094.

[29] K. Tamura, K. N. Radzak, R. E. Vogelpohl, B. A. Wisthoff, Y. Oba, R. K. Hetzler, C. D.

Stickley, *Gait Posture* **2017**, *58*, 108.

[30] R. Matsuzaki, M. Ueda, M. Namiki, T.-K. Jeong, H. Asahara, K. Horiguchi, T. Nakamura, A. Todoroki, Y. Hirano, *Sci. Rep.* **2016**, *6*, 23058.

[31] R. J. A. Allen, R. S. Trask, *Addit. Manuf.* **2015**, *8*, 78.

[32] M. Konakovic, J. Panetta, K. Crane, M. Pauly, *ACM Trans. Graph.* **2018**, *37*, 1.

[33] A. Clausen, F. Wang, J. S. Jensen, O. Sigmund, J. A. Lewis, *Adv. Mater.* **2015**, *27*, 5523.

[34] P. P. Urban, T. Wolf, M. Uebele, J. J. Marx, T. Vogt, P. Stoeter, T. Bauermann, C. Weibrich, G. D. Vucurevic, A. Schneider, J. Wissel, *Stroke* **2010**, *41*, 2016.

[35] H. Lee, P. Ho, M. A. Rastgaar, H. I. Krebs, N. Hogan, *J. Biomech.* **2011**, *44*, 1901.

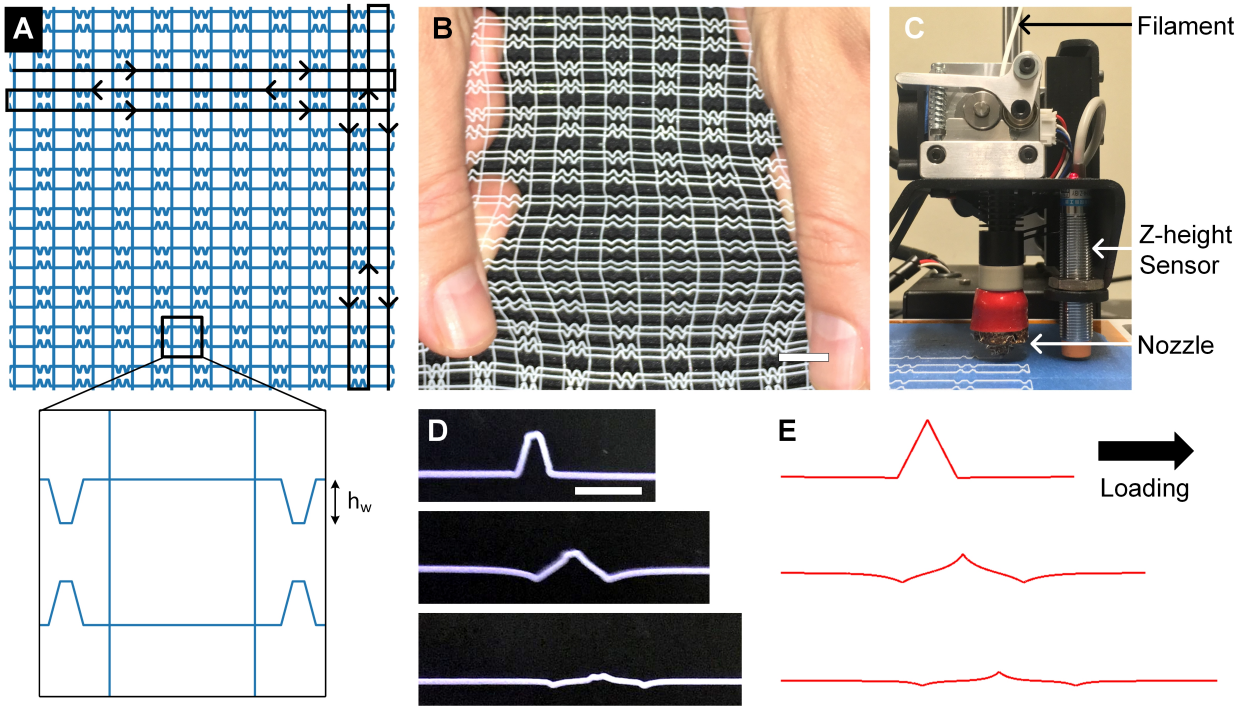

456

457 **Figure 1:** a) Schematic of hierarchical mesh fabrication approach with black lines indicating
458 toolpath; h_w indicates the wave height. b) Exemplary printed mesh (scale bar 10mm). c) Extruder
459 setup used for mesh printing. d) Image of printed fiber with a wave (scale bar 5mm), with
460 increasing tensile strain from top to bottom. e) Finite element simulations of an individual fiber
461 with a wave, with increasing tensile strain from top to bottom.

462
463

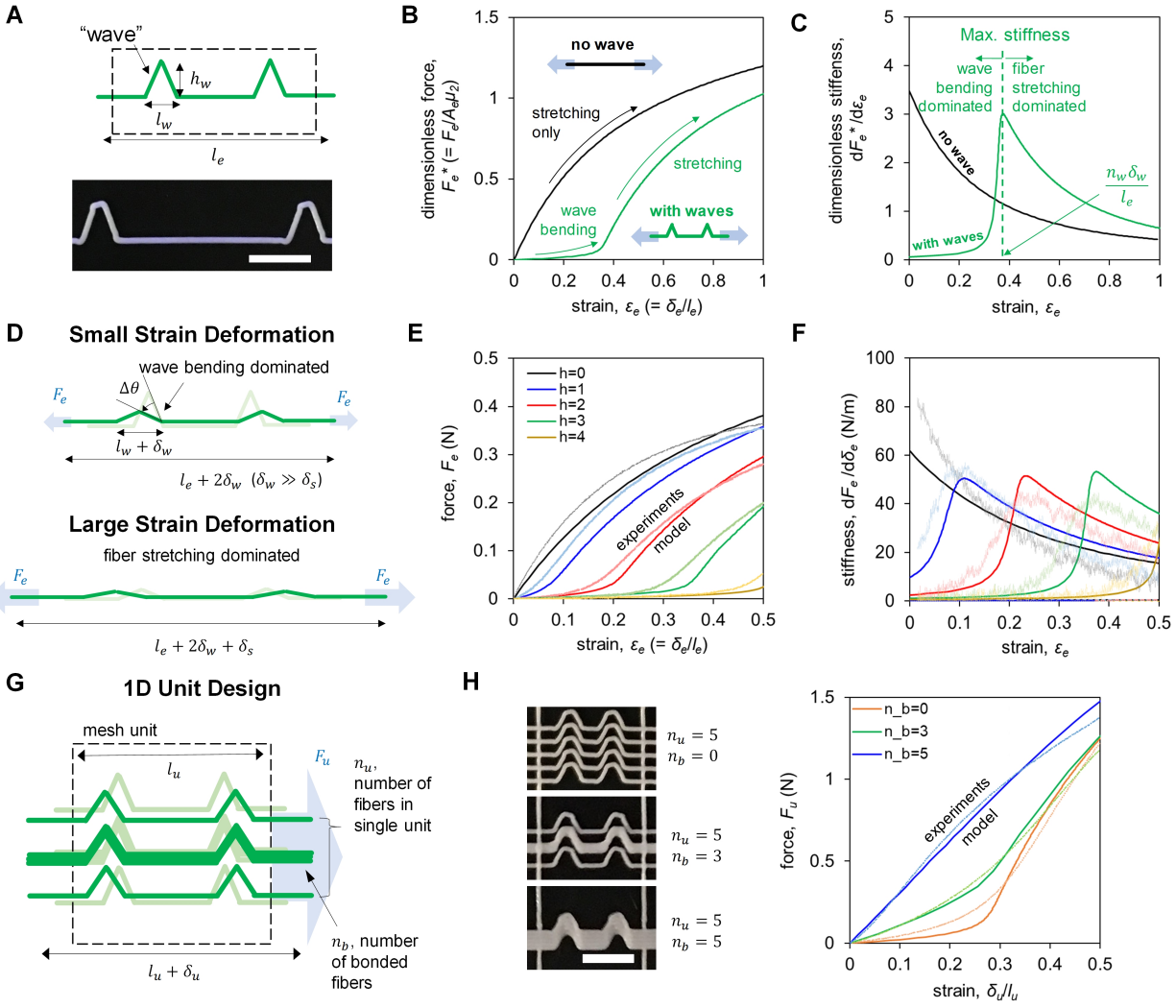

Figure 2: Methods of controlling the non-linear tensile response of individual fibers ("elements"). a) Schematic and image of fiber waves used to introduce non-linear behavior (scale bar is 5mm). b) Mechanical model of tensile response of a fiber with a wave. c) Stiffness of the model fiber in the previous figure d) Schematic describing the mechanical model. e) Controlling the low-to-high strain transition by varying the wave height. f) Stiffness of the fibers versus strain, for the same parameters as in the previous figure. g) Schematic showing variation in fiber bonding for low strain stiffness modulation. h) Images of three exemplary bonded configurations, and corresponding tensile force-displacement curves compared to model.

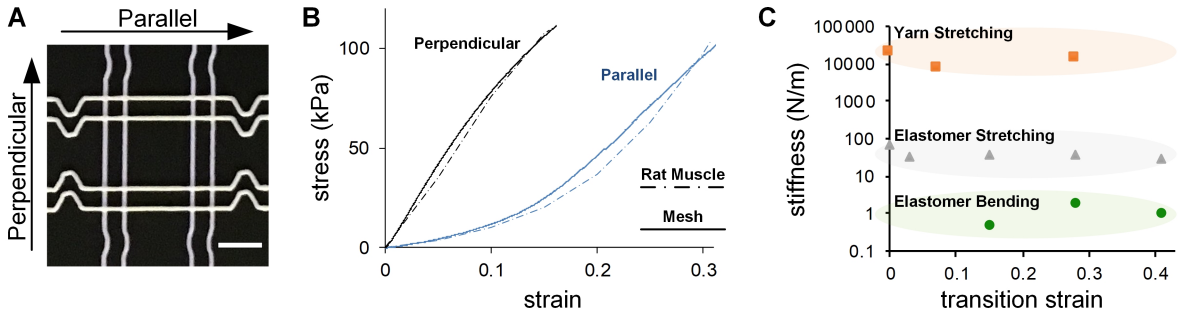

474

475 **Figure 3:** Tailoring mesh mechanics to match tissue. a) image (scale bar 4mm) and b) stress
476 strain data of a mesh unit cell (solid line) whose tensile response in two directions emulates that
477 of muscle tissue as measured by Takaza et al.[21] (dashed line). c) Range of stiffness and transition
478 strains achieved by varying material composition and geometry in the mesh. The stiffness is
479 measured as the approximately linear region before or after the transition from bending to
480 stretching. Yarn stretching refers to incorporation of synthetic fiber, as in Fig. 5.

481

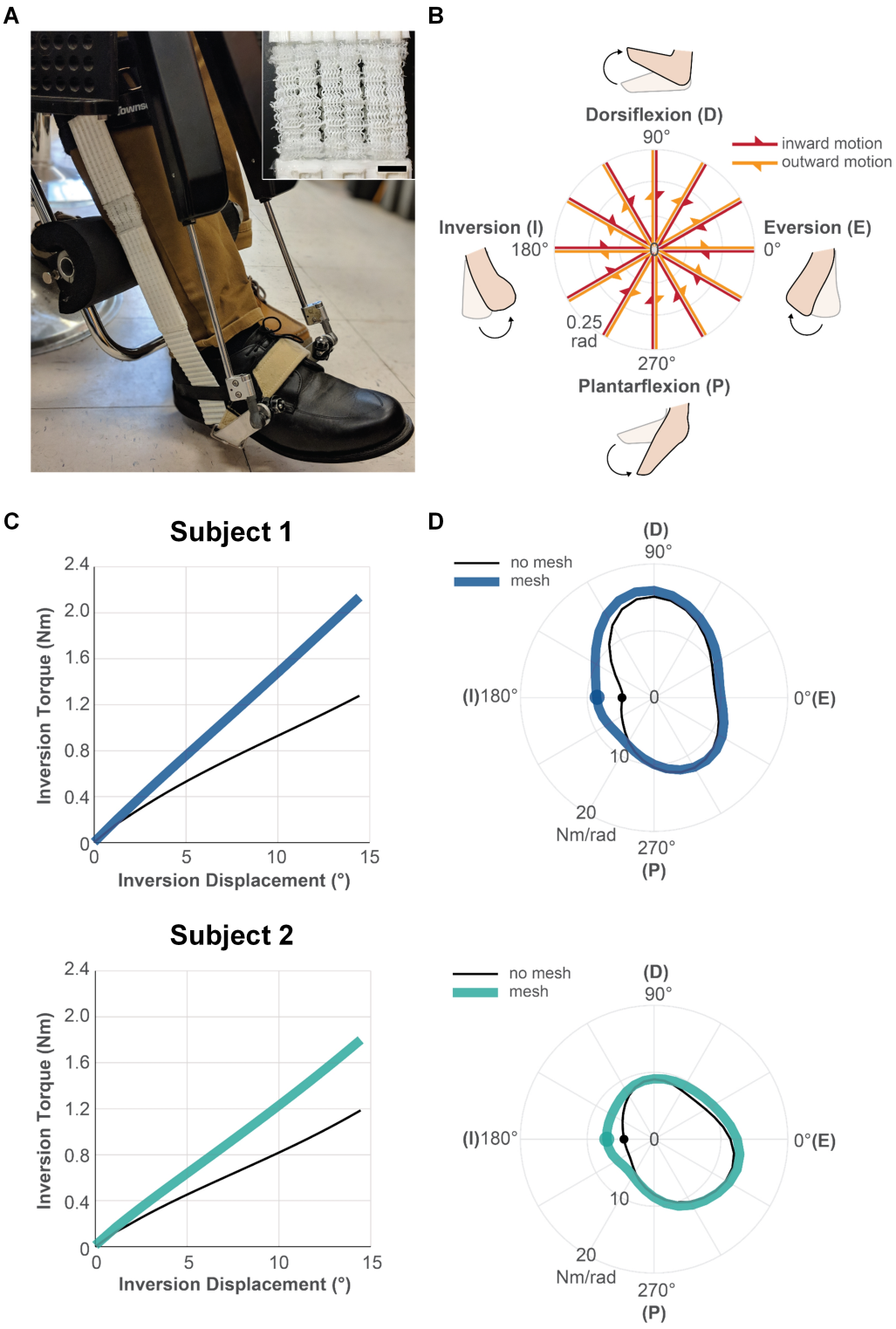

Figure 4: Demonstration of digitally tailored mesh for resisting ankle inversion. a) A non-linear mesh incorporated into an ankle brace and the attachment of this brace to the robot used for ankle stiffness measurement. Inset shows the mesh portion of the brace (scale bar 10mm) b) Schematic

showing the 12 directions the ankle is rotated in in order to generate the stiffness measurements. c) Plots of the torque vs angular displacement in inversion for two human subjects. d) Stiffness distribution in the ankle of these two subjects, with and without the mesh device.

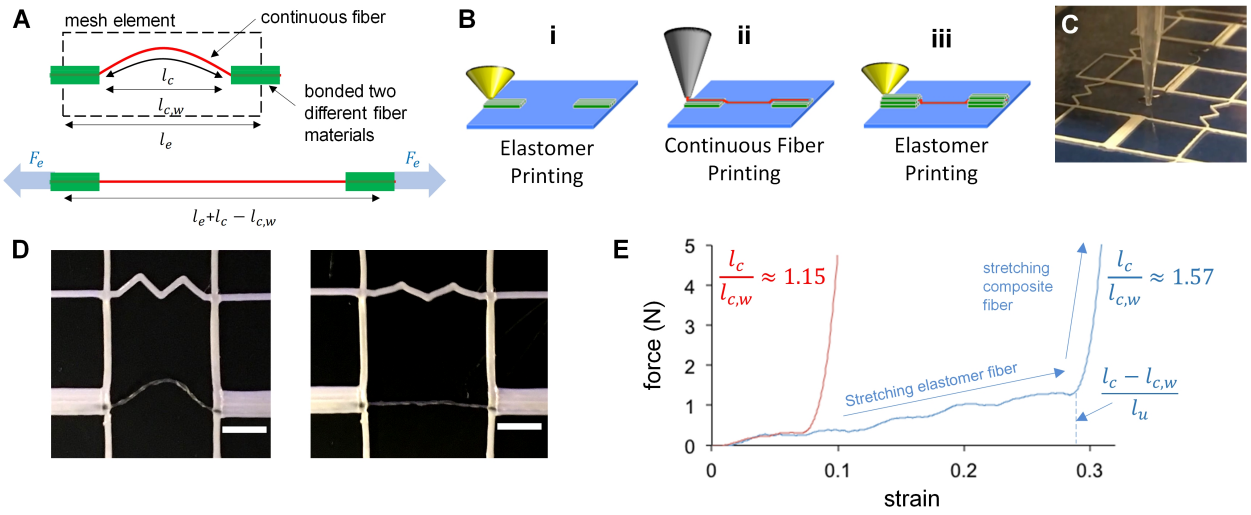

490

491 **Figure 5:** Reinforcing digitally tailored mesh using continuous fiber a) Schematic showing how a
492 stainless steel thread is placed within the bonded elastomer mesh, with a free length of slack. b)
493 Method of patterning continuous fiber mechanism including sandwiching between extruded
494 layers. c) Image of fiber printing. d) Image of unit cell with continuous fiber (scale bar 4mm),
495 unstretched (left) and stretched (right). e) Force-strain curves for two exemplary fiber-reinforced
496 mesh samples, with different initial slack, where l_u denotes the unit cell length (smoothed with
497 Savitzky-Golay filter).

498

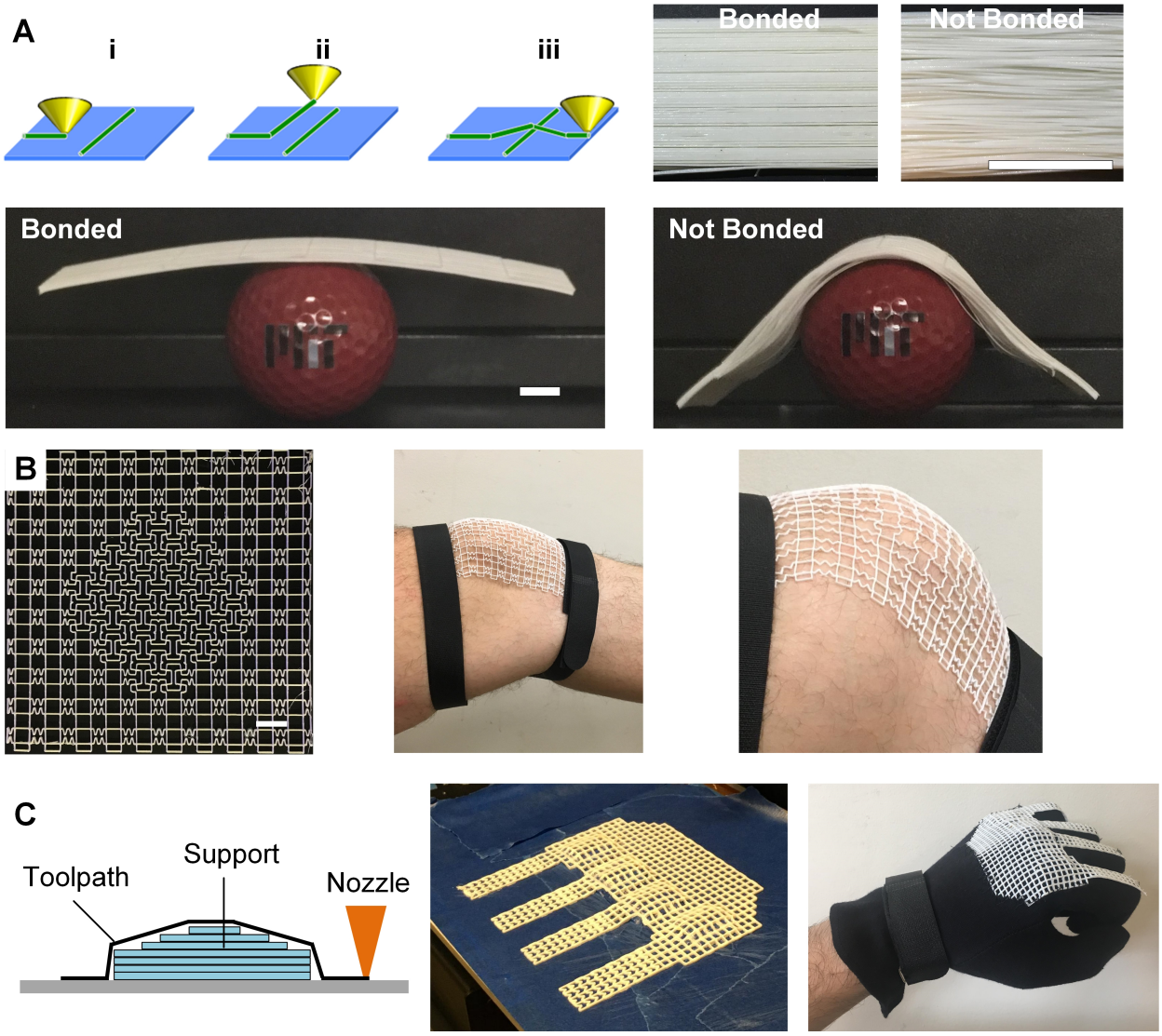

Figure 6: Additional capabilities of mesh printing. a) Modulation of fiber-fiber bonding using 3D toolpaths that allow the fiber to cool before it touches the previous, orthogonally-placed fiber. This results in the non-bonded swatch having noticeably greater drape (scale bar 10mm). b) A mesh (scale bar 10mm) with locally patterned negative Poisson's ratio unit cells, which featuring anisotropic mechanics and showing it's ability to conform to a knee. c) Printing of conformal mesh onto a template, and after which the mesh is sewn onto a glove. This mesh-enhanced glove exerts a restoring force on the fingers when the fist is clenched, as is commonly necessary in stroke rehabilitation.

Explicit toolpath programming in an additive manufacturing process can enable flexible mesh materials with digitally tailored mechanical properties and geometry. The work demonstrates that tensile mesh mechanics can be engineered to match the nonlinear response of muscle, produce an ankle brace with directionally specific inversion stiffness, and presents further concepts for tailoring their 3D geometry for medical applications.

Keyword Additive Manufacturing

Sebastian W. Pattinson,* Meghan E. Huber, Sanha Kim, Jongwoo Lee, Sarah Grunsfeld, Ricardo Roberts, Gregory Dreifus, Christoph Meier, Lei Liu, Neville Hogan, A. John Hart*

Additive Manufacturing of Biomechanically Tailored Meshes for Compliant Wearable and Implantable Devices

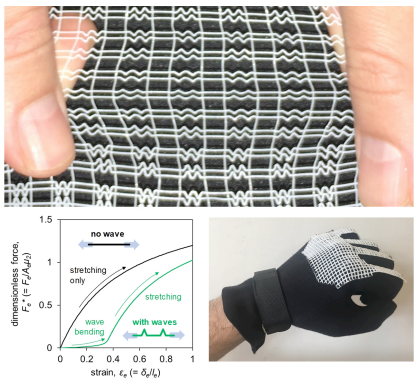

Supporting Information

Additive Manufacturing of Biomechanically Tailored Meshes for Compliant Wearable and Implantable Devices

Sebastian W. Pattinson, Meghan E. Huber, Sanha Kim, Jongwoo Lee, Sarah Grunsfeld, Ricardo Roberts, Gregory Dreifus, Christoph Meier, Lei Liu, Neville Hogan, A. John Hart**

An analytical/numerical model for extension behavior of single element with two waves

Extension by fiber stretching.

For a Mooney-Rivlin material, the engineering stress σ_e under uniaxial extension applied to a single element is expressed as[1]

$$\sigma_e = \left(\mu_1 + \frac{\mu_2}{\lambda_{e,s}}\right)\left(\lambda_{e,s} - \frac{1}{\lambda_{e,s}^2}\right) \quad \text{(Equation S1)}$$

where μ_1 and μ_2 are material constants and $\lambda_{e,s}$ is the element extension by the fiber stretching. Accordingly, the applied force F_e can be given as

$$\frac{F_e}{A_e C_1} = \left(1 + \frac{\mu_2}{\mu_1}\frac{1}{\lambda_{e,s}}\right)\left(\lambda_{e,s} - \frac{1}{\lambda_{e,s}^2}\right) \quad \text{(Equation S2)}$$

where A_e and l_e is the original cross-sectional area and original length of the element respectively. And the extension displacement by stretching can be given as

$$\delta_{e,s} = l_e\left(\lambda_{e,s} - 1\right) \quad \text{(Equation S3)}$$

Extension by fiber bending.

When an element having a wave with height h_w and width l_w is under extension by a tensile force F_e, the fibers at the edges in the wave will bend until the equilibrium angle θ. Assuming the bending stiffness at the edge is constant and given as K', a small amount of bending by increase in tensile force can be expressed as

$$dM_e \cong dF_e \left\{h_w^2 + \left(\frac{l_w}{2}\right)^2\right\}^{1/2} sin\theta \cong -K'd\theta \qquad \text{(Equation S4)}$$

where M_e is the moment at the edge, and θ is the angle of the bended fiber edge. Accordingly, the required force to bend the wave to an angle of θ is given as

$$\int_0^{F_e} dF_e = -K' \left\{h_w^2 + \left(\frac{l_w}{2}\right)^2\right\}^{-1/2} \int_{\theta_0}^{\theta} csc\,\theta\, d\theta \qquad \text{(Equation S5)}$$

$$F_e = K' \left\{h_w^2 + \left(\frac{l_w}{2}\right)^2\right\}^{-1/2} [\log\{\cot\theta + csc\theta\} - \log\{\cot\theta_0 + csc\theta_0\}] \qquad \text{(Equation S6)}$$

where θ_0 is the original angle of the wave edge as

$$\tan\theta_0 = \frac{2h_w}{l_w} \qquad \text{(Equation S7)}$$

Finally, the extension displacement by bending of a fiber element having two waves can be expressed as a function of the equilibrium angle θ as

$$\delta_{e,b} = 4\times \left\{h_w^2 + \left(\frac{l_w}{2}\right)^2\right\}^{1/2} [\cos\theta - \cos\theta_0] \qquad \text{(Equation S8)}$$

By numerical calculation using Eqs. [S2], [S6], [S8], we can acquire force-strain and stiffness-strain curves for a known values of material constant μ_1 and μ_2, bending stiffness K', element length l_e, element cross-sectional area A_e, wave width l_w. Table S1 shows the values used for the plots in Fig. 2a.

564

565 Table S1. Input values for the model estimation.

Input Variables	μ_1	μ_2	K'	l_e	A_e	l_w
Units	MPa	MPa	N·mm	mm	mm^2	mm
Values	0.1	0.54	0.1	24	0.79	2.5

566

567

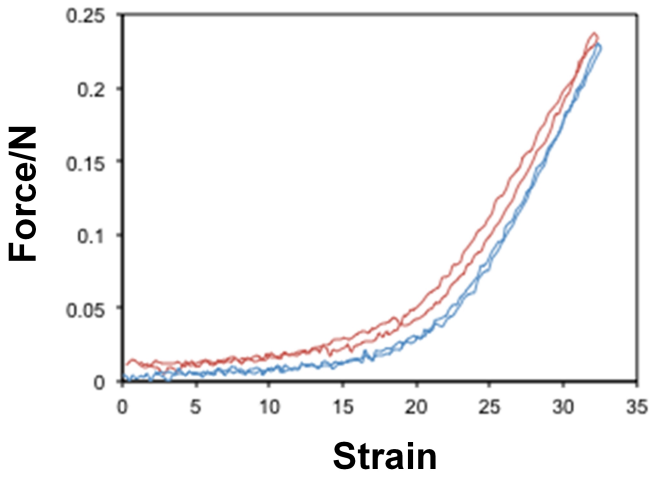

568

569 **Figure S1**: Fatigue behavior of an individual fiber stretched to 32% strain once (red) and 1835

570 times (blue).

571

572

573

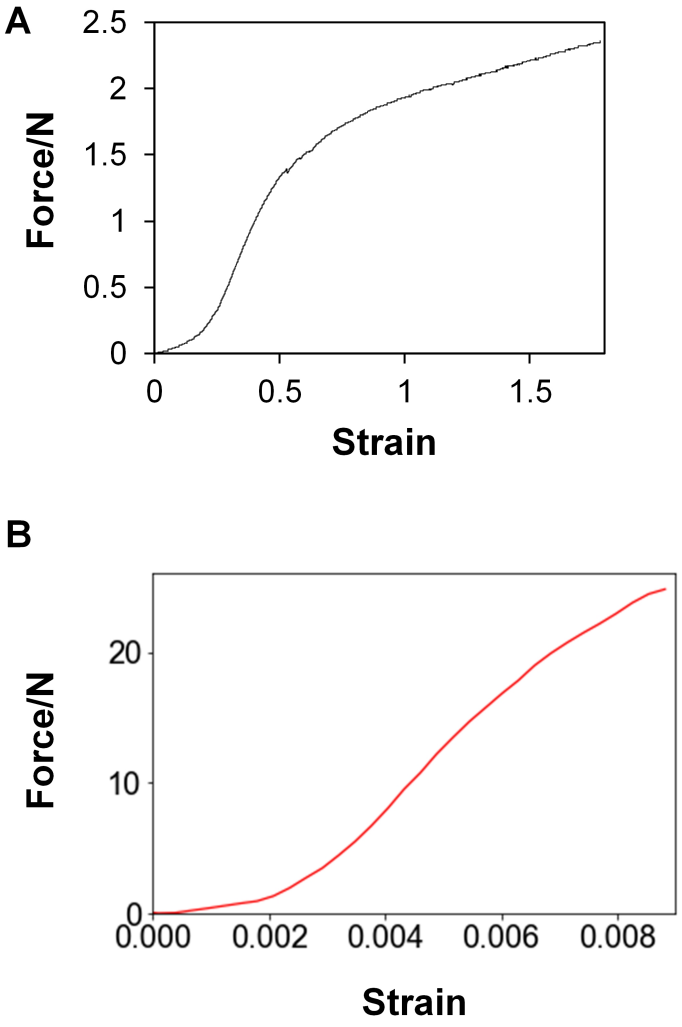

574

575

576 **Figure S2:** a) All-elastomer unit cell mesh tensile test to failure. b) Unit cell with straight

577 continuous fiber tensile test to failure (smoothed with Savitzky-Golay filter).

578

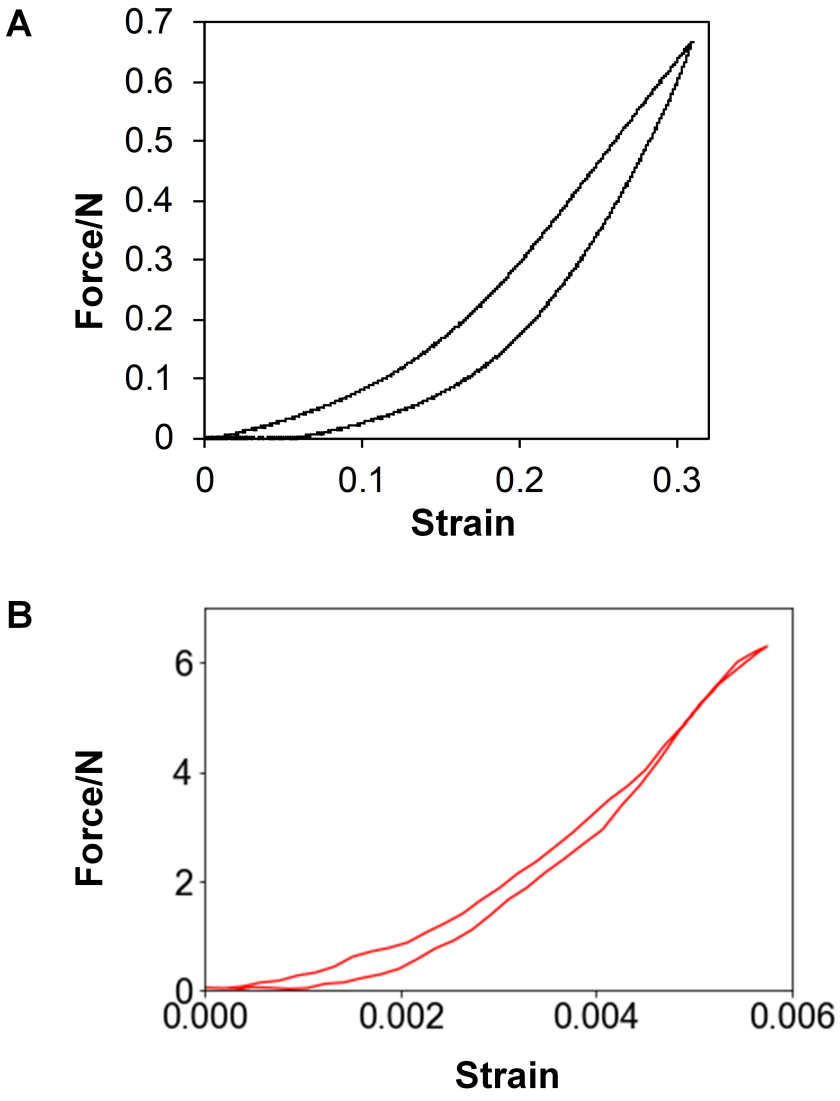

579

580

581 **Figure S3:** a) All-elastomer unit cell mesh single load-unload cycle. b) Unit cell with straight

582 continuous fiber single load-unload cycle (smoothed with Savitzky-Golay filter).

583

584

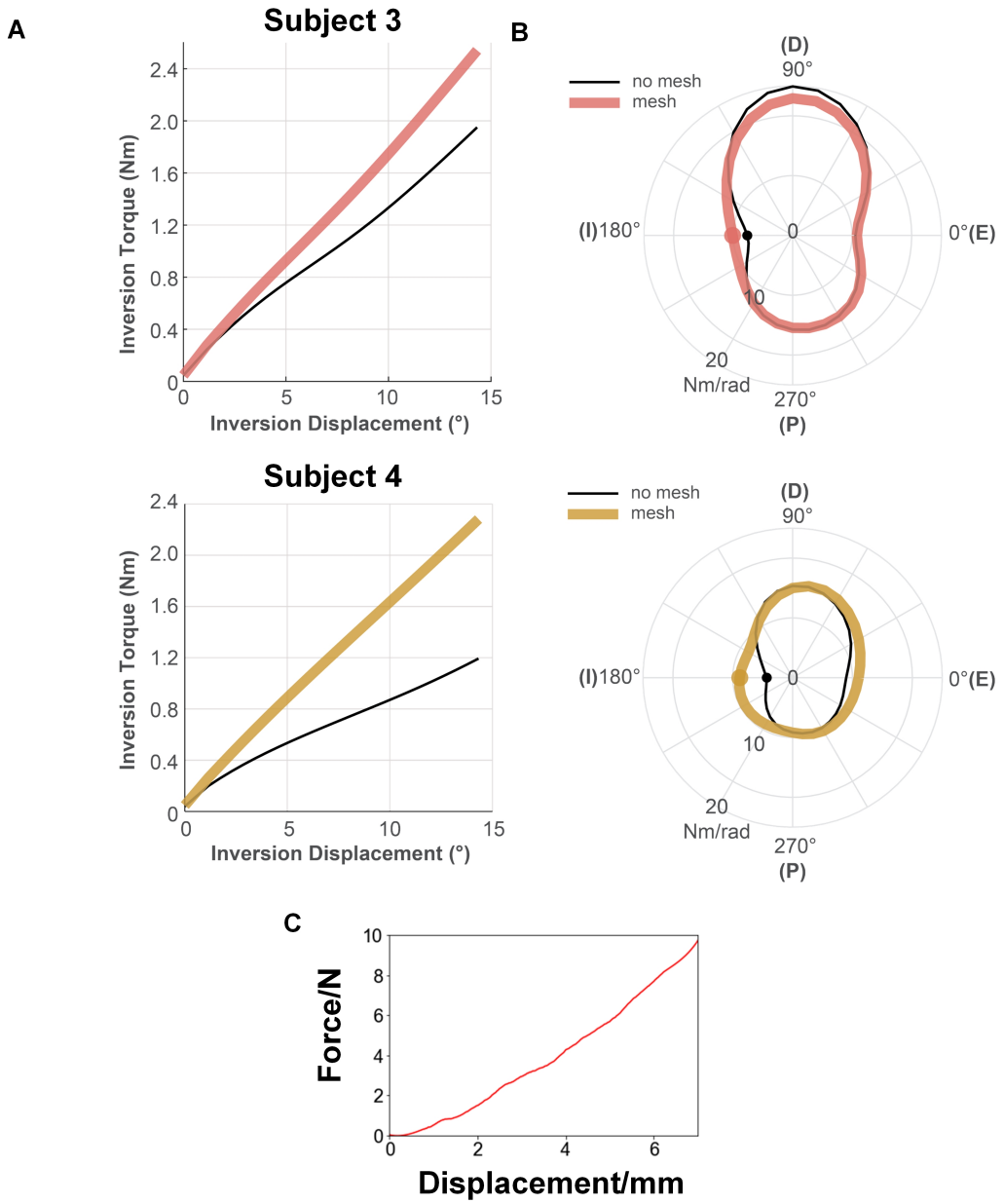

585

586 **Figure S4:** a) Plots of the torque vs angular displacement in inversion for further two human

587 subjects. b) Stiffness distribution in the ankle of these two subjects. c) Force vs. displacement

588 curve for the ankle brace (smoothed with Savitzky-Golay filter).

589

590 **Supporting Reference**

591 [1] A. Bower, Applied Mechanics of Solids; CRC Press, 2009